ORIGINAL ARTICLE

Integrating large specific surface area and high conductivity in hydrogenated NiCo$_2$O$_4$ double-shell hollow spheres to improve supercapacitors

Xiaoming Li[1,2,4], Lianfu Jiang[1,2,4], Cheng Zhou[3], Jinping Liu[3] and Haibo Zeng[1,2]

Increasing specific surface area and electrical conductivity are two crucial ways to improve the capacitive performance of electrode materials. Nanostructure usually enlarges the former but reduces the later; thus, it is still a great challenge to overcome such contradiction. Here, we report hydrogenated NiCo$_2$O$_4$ double-shell hollow spheres, combining large specific surface area and high conductivity to improve the capacitive performance of supercapacitors. The specific surface area of NiCo$_2$O$_4$ hollow spheres, fabricated via programmed coating of carbon spheres, was enlarged 50% (from 76.6 to 115.2 m^2 g^{-1}) when their structure was transformed from single-shell to double-shell. Furthermore, activated carbon impedance measurements demonstrated that the low-temperature hydrogenation greatly decreased both the internal resistance and the Warburg impedance. Consequently, a specific capacitance increase of $>62\%$, from 445 to 718 F g^{-1}, was achieved at a current density of 1 A g^{-1}. Underlying such great improvement, the evolution of chemical valence and defect states with co-increase of these two factors was explored through X-ray photoelectron spectroscopy. Moreover, a full cell combined with NiCo$_2$O$_4$ and AC was assembled, and an energy density of 34.8 Wh kg^{-1} was obtained at a power density of 464 W kg^{-1}.
NPG Asia Materials (2015) **7**, e165; doi:10.1038/am.2015.11; published online 13 March 2015

INTRODUCTION

Supercapacitors, also known as electrochemical capacitors, have attracted great attention because of their outstanding power density, long cycling life and fast charge/discharge ability.[1–3] These virtues make them remarkable candidates for the electrical sources of hybrid electric vehicles, for which strong explosiveness is highly desired. Principally, supercapacitors run according to ion adsorption (electrochemical double-layer capacitors) or fast Faradaic reactions (pseudocapacitors) mechanisms. Comparatively speaking, the former has low specific capacitance and hence hard to satisfy the growing demand of peak-power assistance in electric vehicles.[4] Thus, more and more attentions were focused on pseudocapacitive electrode materials because their energy density associated with Faradaic reactions is much larger than that of electrochemical double-layer capacitors.[5–8]

To improve performances of pseudocapacitors, two crucial factors are usually considered for the electrode materials, they are large specific surface area and high conductivity for electrolyte ions and electrons. On the one hand, large specific surface area will provide more electroactive sites for the Faradaic reactions, and load more double-layer charges. Along such idea, many kinds of nanomaterials,[9–11] especially hollow spheres,[12] have been developed to improve pseudocapacitors, but the increased contact resistance often emerges in these porous materials. On the other hand, increasing conductivity will greatly favor the Faradaic reactions, which has been demonstrated typically in the integration of oxides with metal foam,[13] carbon cloth,[9] graphene and carbon nanotubes.[14] However, these methods do not change the intrinsic properties of the metal oxides.[15,16] Therefore, achieving the co-existence of large specific surface area and high conductivity in metal oxides themselves has been desired.

Here, taking hydrogenated NiCo$_2$O$_4$ double-shell hollow spheres as an example, we demonstrate the improvement of supercapacitors by the co-improved specific surface area and conductivity. Compared with single-shell spheres, double-shell spheres, fabricated by programmed coating of carbon spheres, have 50% larger specific surface area and remarkably reduced resistance after hydrogenation at the same time. Besides the prospective contribution to the specific surface area owing to the hierarchical porosity, the incremental shells intercross with each other, and hence provide more and shorter ion/electron diffusion paths. Such collective optimization really brings the significant promotion of the specific capacitance from 445 to 718 F g^{-1} with an amplification of 62% at a current density of 1 A g^{-1}.

[1]State Key Laboratory of Mechanics and Control of Mechanical Structures & College of Materials Science and Technology, Nanjing University of Aeronautics and Astronautics, Nanjing, China; [2]Institute of Optoelectronics & Nanomaterials, College of Materials Science and Engineering, Nanjing University of Science and Technology, Nanjing, China and [3]Institute of Nanoscience and Nanotechnology, Department of Physics, Central China Normal University, Wuhan, China
[4]These authors contributed equally to this work.
Correspondence: Professor HB Zeng, Institute of Optoelectronics & Nanomaterials, College of Materials Science and Engineering, Nanjing University of Science and Technology, Nanjing, Jiangsu 210094, China.
E-mail: zeng.haibo@njust.edu.cn

EXPERIMENTAL PROCEDURE

Preparation of $NiCo_2O_4$ double and single-shell hollow spheres

Synthesis of carbon spheres. The carbon spheres were prepared according to previous report.[17] In total, 6.93 g sucrose was dissolved in 70 ml distilled water and stirred with a magnetic stirrer to obtain a clear solution. Then the solution was transferred into a Teflon-lined autoclave of 100 ml capacity and kept at 190 °C for 2 h. When the reaction finished, the reactors were cooled to room temperature naturally. The black products were collected by centrifugation and washed with distilled water then ethanol several times. Finally, the products were dried at 60 °C for 12 h.

Synthesis of $NiCo_2O_4$ hollow microspheres. In all, 0.36 g carbon spheres were dispersed in 70 ml $Ni(NO_3)_2·6H_2O$ (0.29 g) and $Co(NO_3)_2·6H_2O$ (0.58 g) solution by stirring for 1 h to ensure that metal ions can be sufficiently adsorbed on the surface of carbon spheres. Then urea (1.25 g) was added and kept stirring for 1 h. After that, the black solution was transferred into a flask and reacted at 90 °C for 4 h. When the reaction finished, the suspension was cooled to room temperature and centrifuged to obtain the $NiCo_2(OH)_6$/C precursors. The black products were washed with ethanol and dried at 60 °C for 12 h. Then, the precursors were annealed at 400 °C for 4 h with a heating rate of 2 °C min^{-1}. Single-shelled $NiCo_2O_4$ hollow spheres were obtained and named as S-$NiCo_2O_4$. To obtain double-shelled spheres (named as D-$NiCo_2O_4$), above processes with the same precursor concentration were repeated. In addition, precursors of D-$NiCo_2O_4$ were heated at 400 and 300 °C for 4 h with the same heating rate to find the effects of annealing temperatures on electrochemical properties.

Materials characterization

X-ray diffraction (XRD) patterns were recorded on a multipurpose XRD system D8 Advance from Bruker with a Cu Kα radiation ($\lambda = 1.5406$ Å). The morphologies and structures were observed with field-emission scanning electron microscopy (FEI Quanta 250FEG). The Brunauer-Emmett-Teller surface area of the samples was determined from nitrogen adsorption and desorption isotherms, measured at the temperature of liquid nitrogen on a Micromeritics-3Flex (USA) surface area analyzer. X-ray photoelectron spectroscopy analysis was carried out on an ARL-9800 instrument with a monochromatic X-ray source AlKa excitation (1486.6 eV).

Electrochemical measurements

The working electrodes were prepared with $NiCo_2O_4$, acetylene black and polytetrafluoroethylene in a weight ratio of 80:15:5. The slurry combined with the mixture and distilled water was coated on nickel foam and dried at 60 °C for 12 h. The as-prepared electrodes were then subjected to a pressure of 5 MPa for the following electrochemical tests by cyclic voltammetry (CV) and chronopotentiometry measurements performed on a CHI604D electrochemical analyzer (Shanghai Chenhua Instrument Co., Shanghai, China). The loading mass of active material is in the range of 3–5 mg cm^{-2}, which is 5.28, 4, 3.5,

3.76 mg cm^{-2} for S-$NiCo_2O_4$–400 °C, D-$NiCo_2O_4$–400 °C, D-$NiCo_2O_4$–300 °C, D-$NiCo_2O_4$–300 °C-H, respectively. All the measurements were carried out in a three-electrode system with a working electrode, a platinum plate counter electrode and a saturated calomel electrode reference electrode at room temperature. The electrolyte used here was 6 M potassium hydroxide aqueous solution. The specific capacitance of the electrode materials is calculated from the charge–discharge curves according to the equation of $C_s = It/\Delta V$, Where C_s is the specific capacitance (F g^{-1}), I donates the discharge current (A g^{-1}), t is the discharging time and ΔV is the discharging interval (V). The performances of the electrodes in three-electrode system in this work are the results after subtracting the effect of the substrate.

For the fabrication of asymmetric supercapacitor, an activated carbon (AC) electrode was prepared by mixing 80 wt% AC and 20 wt% PVA. The mixture was casted onto nickel foam. This electrode played as negative electrode and was pressed and combined with the positive electrode with 6 M potassium hydroxide as the electrolyte to assemble the full cell. The mass of positive and negative material was decided according to the well-known charge balance theory. The mass of positive and negative materials were 3.1 and 6.1 mg cm^{-2}, respectively.

RESULTS AND DISCUSSION

Double-shell structure and resulted larger specific surface area

The synthetic schematic is shown in Figure 1a. In brief, the single-shell and double-shell spheres were fabricated by one-cycle and two-cycle coating of the $NiCo_2(OH)_6$ intermediate materials on carbon sphere templates, respectively. More specifically, uniform carbon spheres (Figure 1b) were prepared firstly to be subsequently used as templates. Then, appropriate amounts of Ni^{2+} and Co^{2+} precursors were added into the solution containing carbon spheres to form the $NiCo_2(OH)_6$/C composites under the assistance of urea. After calcination, $NiCo_2O_4$ single-shelled hollow (denoted as S-spheres) spheres can be obtained if only one-cycle $NiCo_2(OH)_6$ coating was applied. But when above procedures were repeated, the products were double-shelled hollow spheres (denoted as D-spheres). The involved chemical reactions can be described by the following four equations:
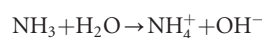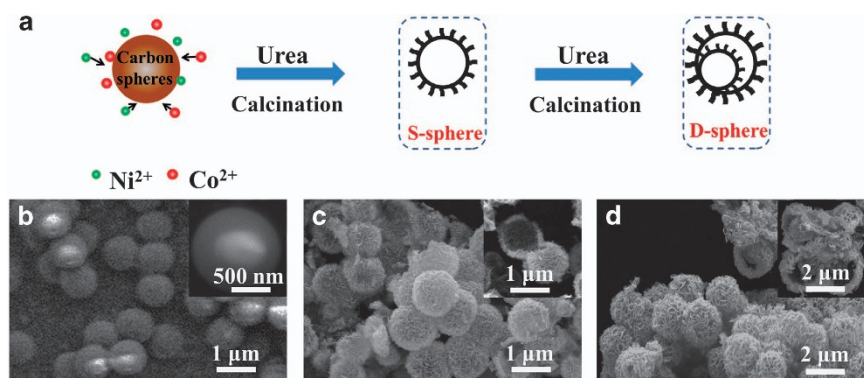
$$6CO(NH_2)_2 \rightarrow C_3N_6H_6 + 6NH_3 + 3CO_2$$

$$NH_3 + H_2O \rightarrow NH_4^+ + OH^-$$

$$Ni^{2+} + 2Co^{2+} + 6OH^- \rightarrow NiCo_2(OH)_6$$

$$NiCo_2(OH)_6 + 1/2O_2 \rightarrow NiCo_2O_4 + 3H_2O$$

Figure 1c shows the scanning electron microscopy image of $NiCo_2O_4$ single-shelled hollow spheres, which exhibit very uniform spherical morphology. The particles have an average size of ~1 μm,

Figure 1 Fabrication of $NiCo_2O_4$ double-shell spheres. (**a**) Synthetic scheme of $NiCo_2O_4$ hollow spheres, the single-shell and double-shell spheres were fabricated by one-cycle and two-cycle coating of the $NiCo_2(OH)_6$ intermediate material on carbon sphere templates, respectively. (**b**) Primal carbon spheres used as templates. (**c**), Single-shell hollow spheres. (**d**) double-shell hollow spheres.
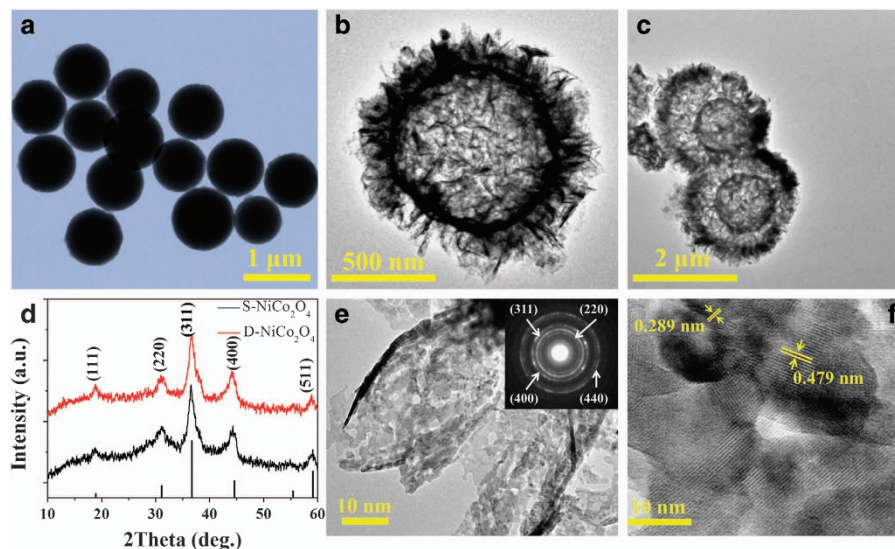
Figure 2 Microstructure of $NiCo_2O_4$ single-shell and double-shell spheres. TEM images of (**a**) carbon spheres, (**b**) single-shelled and (**c**) double-shelled $NiCo_2O_4$ spheres. (**d**) XRD patterns of the as-prepared hollow $NiCo_2O_4$ spheres. High-resolution TEM images (**e**, **f**) of the sheets and corresponding SAED result.
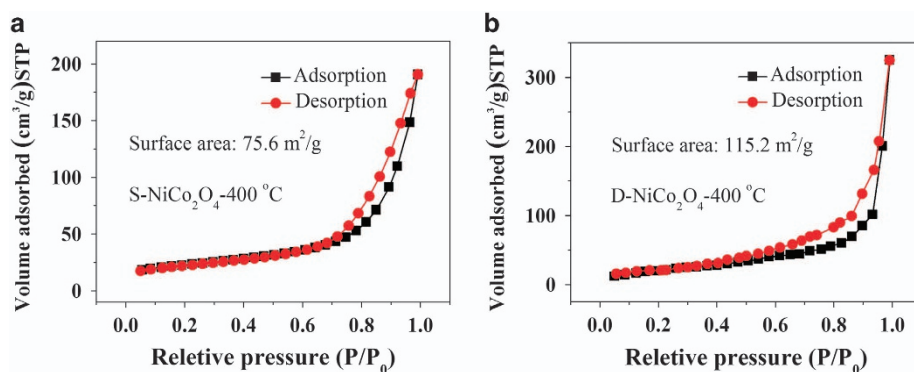

Figure 3 Increased specific surface area of $NiCo_2O_4$ double-shell spheres. Nitrogen adsorption–desorption isotherms of single-shelled (**a**) and double-shelled (**b**) $NiCo_2O_4$ spheres.

which is similar to that of the carbon spheres. Compared with the smooth surface of carbon spheres in Figure 1b, the shell of S-spheres is rough and consists of $NiCo_2O_4$ nanosheets, which provide large specific surface. This sheet-like structure is further confirmed by the high-resolution scanning electron microscopy image (Supplementary Figure S1). Obvious hollow structure can be observed as shown in Figure 1c inset. After the repeat of reaction and calcination, D-spheres were obtained with larger size, as shown in Figure 1d. The $NiCo_2O_4$ sheet-consisted shell is clearer. Significantly, small balls can be clearly seen inside bigger cracked balls, as shown in Figure 1d inset, which gives a solid evidence for the formation of double shells.

Figure 2a shows the transmission electron microscopy image of carbon spheres, which exhibit uniform size with spherical shape. The hollow interior and geometrical structure of the $NiCo_2O_4$ products based on these carbon spheres were further analyzed with transmission electron microscopy examination. The single- and double-shelled structures can be seen clearly from Figures 2b, c. All the shells are composed of loose nanosheets, which agree well with the scanning electron microscopy results. The XRD patterns of single- and double-shelled spheres are shown in Figure 2d, and can be well indexed to the spinel structure (JCPDS card no. 20-0781) of $NiCo_2O_4$ without any

residues or contaminants, indicating the high purity. Figures 2e, f are the high-resolution transmission electron microscopy images of a sheet. Obviously, the sheets are porous and composed of nanocrystals with size in the range of several to tens of nanometers. Such polycrystalline structure can also be confirmed by the selected area (electron) diffraction image shown in Figure 2e inset. The pores in the sheet are smaller than 10 nm. Therefore, the loose and porous sheet structure provides not only larger specific areas but also more connected transport channels for electrolyte ions, which will improve the specific capacitance from both aspects. Besides, no recognizable carbon species can be found, indicating the complete removal of the carbon templates, which is in good agreement with the XRD patterns.

To investigate whether the specific area is enlarged as expected with the increase of shell number, N_2 adsorption–desorption measurements were carried out on them. The adsorption isotherms are shown in Figure 3. All the isotherm profiles can be classified as type IV[12] and hysteresis loops are observed in the range of $0.7–1.0$ P/P_0 (Figure 3a) and $0.5–1.0$ P/P_0 (Figure 3b), suggesting that the as-prepared samples have a typical mesoporous structure, which can be further supported by the Barrett–Joyner–Halenda pore size distribution (Supplementary Figure S2). Results demonstrate that most of the
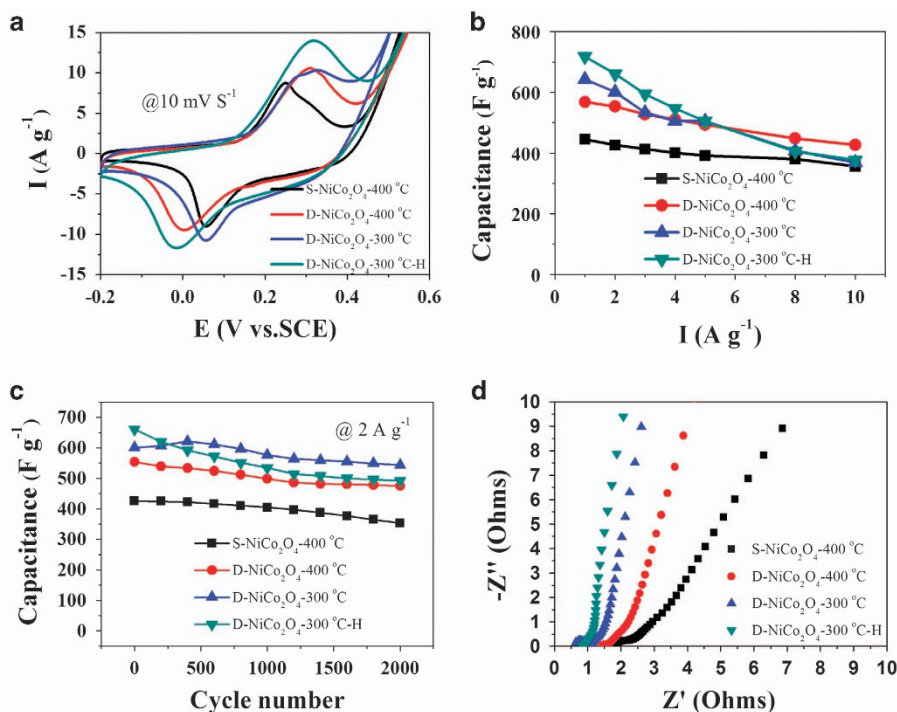
Figure 4 Performances of $NiCo_2O_4$ double-shell sphere-based supercapacitors. (**a**) CV curves of different samples at a scan rate of $10\,mV\,S^{-1}$. (**b**) Calculated specific capacitances of different samples as a function of current density. (**c**) Cycling performance of different electrodes as a function of cycle number at $2\,A\,g^{-1}$. (**d**) Nyquist plots of different samples. (It means that the sample was annealed at $300\,°C$ and hydrogenated at $300\,°C$ for $D-NiCo_2O_4$–$300\,°C$ and $D-NiCo_2O_4$–$300\,°C$-H, respectively).

pores are smaller than 10 nm. The measured Brunauer-Emmett-Teller specific surface areas are 76.6 and $115.2\,m^2\,g^{-1}$ for $S-NiCo_2O_4$ and $D-NiCo_2O_4$, respectively. Apparently, the specific surface area was indeed increased significantly as we expected. Such hierarchical hollow structures with large surface area, and intriguing mesoporosity can offer sufficient electron-active sites and transport channels to facilitate more electrochemical reactions in the redox process, resulting in improved specific capacitance.

Increased capacitive performance of double-shell structure
$NiCo_2O_4$ has a spinel structure in which Ni atoms occupy the octahedral sites, and Co atoms are distributed over both octahedral and tetrahedral sites.[9] Remarkably, both Ni and Co cations possess two kinds of valence states, +2 and +3, respectively. Such mixed valence states make $NiCo_2O_4$ possess high electrical conductivity because the activation energy of electron transfer is relatively low.[18] It has been reported that the conductivity of a single crystal $NiCo_2O_4$ nanoplate can be as high as $62\,S\,cm^{-1}$ at $300\,K$.[18] Such outstanding electrical conductivity provides promising presupposition for $NiCo_2O_4$ to act as high-capacitance electrode in pseudocapacitors, but how to design $NiCo_2O_4$ nanostructures with high large specific areas, such as multi-shelled hollow spheres, is still in a great challenge for practical applications.

The as-prepared single-shelled and double-shelled $NiCo_2O_4$ hollow spheres were used to fabricate the pseudocapacitive electrodes to evaluate their electrochemical properties in a three-electrode system. CV and galvanostatic charge–discharge measurements were carried out. First of all, CV measurements of bare nickel foam were conducted to subtract the effect of the substrate to get the real capacitance (Supplementary Figure S3). The specific capacitances of nickel foam under a scanning rate of $5\,mV\,s^{-1}$ are calculated according to the

loading mass as shown in Supplementary Table S4. We can see that nickel foam makes a contribution of ~3% to the specific capacitance. Therefore, all the results in this work are the real capacitance of electrode materials after subtracting the contribution of nickel foam. For the convenience of comparison, typical CV curves of all the samples swept from $-0.2\,V$ to $0.6\,V$ at the scanning rate of $10\,mV\,S^{-1}$ are shown in Figure 4a. The detailed CV and galvanostatic charge–discharge curves of $S-NiCo_2O_4$ and $D-NiCo_2O_4$ are shown in Supplementary Figure S5. The CV curves with a couple of redox peaks imply that the capacitance of $NiCo_2O_4$ mainly results from the contribution of Faradaic pseudocapacitor because the shape of CV curve for electrochemical double-layer capacitors is normally close to an ideal rectangle. As the scan rate increases from 5 to $25\,mV\,S^{-1}$, the current increases while the shape changes little (Supplementary Figure S5), indicating the good electrochemical capacitive nature. The redox peaks within the scanning range are mainly resulted from Faradaic reactions related to M–O/M–O–OH, where M refers to Co and Ni, including following reactions:[12]

$$NiCo_2O_4 + OH^- + H_2O \leftrightarrow NiOOH + 2CoOOH + e^-$$
$$CoOOH + OH^- \leftrightarrow CoO_2 + H_2O + e^-$$
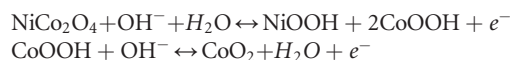
In addition, the area surrounded within the CV curve of $D-NiCo_2O_4$ is obviously larger than that of $S-NiCo_2O_4$, indicating the better capacitance of $D-NiCo_2O_4$.

To further quantify the supercapacitance, galvanostatic charge–discharge measurements with a potential window of 0–0.4 V were conducted at various current densities ranging from 1 to $10\,A\,g^{-1}$ (Supplementary Figure S5). The specific capacitances of the electrodes can be calculated based on the charge–discharge curves and the results are collected in Figure 4b. Impressively, the capacitance increases from 445 of $S-NiCo_2O_4$ to $568\,F\,g^{-1}$ of $D-NiCo_2O_4$ at the current density of
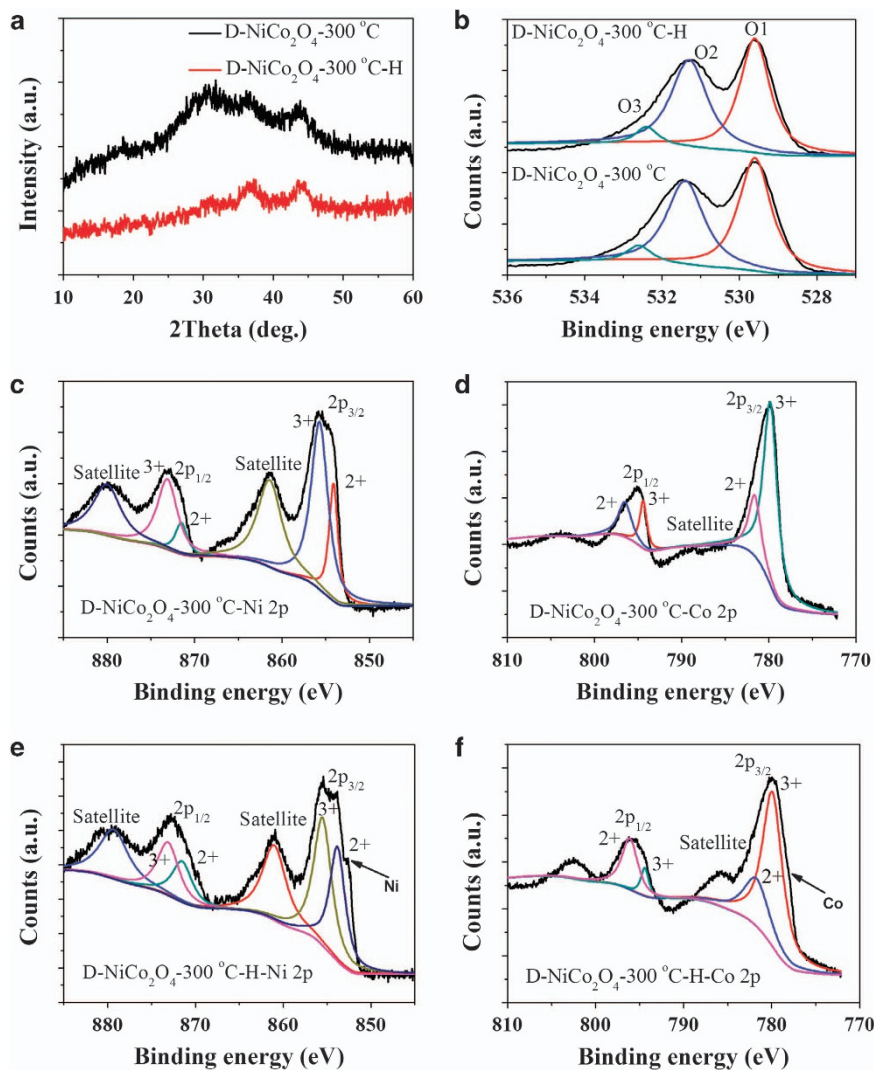
Figure 5 Chemical states inside $NiCo_2O_4$ double-shell spheres. (**a**) XRD and (**b**) O 1 s patterns of samples annealed at 300 °C and in hydrogen. High-resolution XPS spectra of (**c**) Ni 2p and (**d**) Co 2p for $NiCo_2O_4$ annealed at 300 °C. High resolution XPS spectra of (**e**) Ni 2p and (**f**) Co 2p for hydrogenated $NiCo_2O_4$.

$1 A g^{-1}$, which can be assigned to the increase of electroactive sites owing to larger specific surface. Nearly 80% capacitance was maintained for both of the electrodes at a high current density of $10 A g^{-1}$. Considering that cycle stability is also a very important factor to evaluate the performance of electrodes, the continuous charge–discharge performance was measured for 2000 cycles under a current density of $2 A g^{-1}$, as shown in Figure 4c. In all, 82.9% (S-$NiCo_2O_4$) and 85.8% (D-$NiCo_2O_4$) of their initial capacitances can be retained after 2000 cycles, indicating the excellent capacitance retention.

The influence of annealing temperature was also investigated because annealing behaviors affected the performance greatly, and high-temperature treatment would lead to degraded performance sometimes.[19] Annealing treatments at different temperatures and under different atmospheres were conducted and the results are shown in Figure 4 (detailed information is shown in Supplementary Figure S6). From Figure 4b we can see that low-temperature treatment resulted in higher specific capacitance at low current density, whereas it decreased quickly at higher current density. Despite this, the capacitance retention (90.5%) is much better than that of samples annealed at 400 °C. Interestingly, the capacitance gradually increases

after 400 cycles, in contrast with most cycle stability tests. It means that additional 400 cycles are needed to fully activate the electrode. Besides, as we discussed above, improving the electrical conductivity of electrode is another approach to improve the capacitive performance. For TiO_2-related electrodes, hydrogenation has led to excellent performance owing to the formation of Ti^{3+} and oxygen vacancy, which provides excess electrons for ameliorative electrical property.[20] Inspired by this, the samples annealed at 300 °C were further treated in hydrogen at 300 °C for 1.5 h. Interestingly, the specific capacitance increased to $718 F g^{-1}$ at a current density of $1 A g^{-1}$ and the high current density performance is also better than the sample annealed at 300 °C. However, the capacitance retention is not such good, whereas the specific capacitance is still higher than high-temperature-annealed samples.

To investigate the electrical properties of the samples treated under different annealing temperature and atmosphere, AC impedance measurements were carried out. Figure 4d shows typical Nuquist plots of the four samples measured in an open-circuit condition. At high frequency, the point intersecting with the real axis exhibits an internal resistance and the linear part at low frequency delivers the

Warburg impedance involved in the diffusion of electrolyte ions. We can see that the hydrogenated sample possesses the lowest internal resistance, which indicates the improvement of material's electrical conductivity resulted from hydrogenation treatment. In addition, low-temperature annealed samples also possess better electrical conductivity than that of samples treated at high temperature. For ideal supercapacitors, the impedance plot is a line perpendicular to the real axis and the hydrogenated sample exhibited largest slope (the slopes of straight lines of the four samples are 57.6°, 74.2°, 79.8° and 82.4°, respectively).

What's the underlying mechanism for the greatly improved performance after low-temperature annealing and hydrogenation? Generally, electrical properties are related to the material's structure. Therefore, XRD and X-ray photoelectron spectroscopy measurements were conducted on the low-temperature annealed and hydrogenated samples. Figure 5a shows the XRD patterns and we find that the samples possess low crystallinity compared with the two samples annealed at high temperature (Figure 2a). Thus, the increased

capacitance may be assigned to increased defect sites owing to low crystallinity (compared with Figure 2a) when annealed at low temperature.[19] This can also be further supported by O1 s X-ray photoelectron spectroscopy spectra as shown in Figure 5b, which can be fitted with three sub-peaks as O1, O2 and O3. The peak O1 at 529.6 eV is the typical metal–oxygen bonds. The peak O2 at 531.3 eV corresponds to the defects with low oxygen and the peak O3 can be attributed to adsorbed water at or near the surface.[21] The high relative intensity of peak O2 indicates the large amount of defects such as oxygen vacancies at the surface. On the other hand, recent research implies that amorphous structure is commensurate with crystalline materials in supercapacitors owing to the similar reason.[22]

Figures 5c and d are the high resolution X-ray photoelectron spectroscopy spectra of Ni 2p and Co 2p for $NiCo_2O_4$ annealed at 300 °C, respectively. It shows that the surface of the sample has a composition containing Ni^{2+}, Ni^{3+}, Co^{2+} and Co^{3+} with two and one shakeup satellites, respectively.[23] The hydrogenated sample exhibits similar results, except the relative intensities of different valences, as
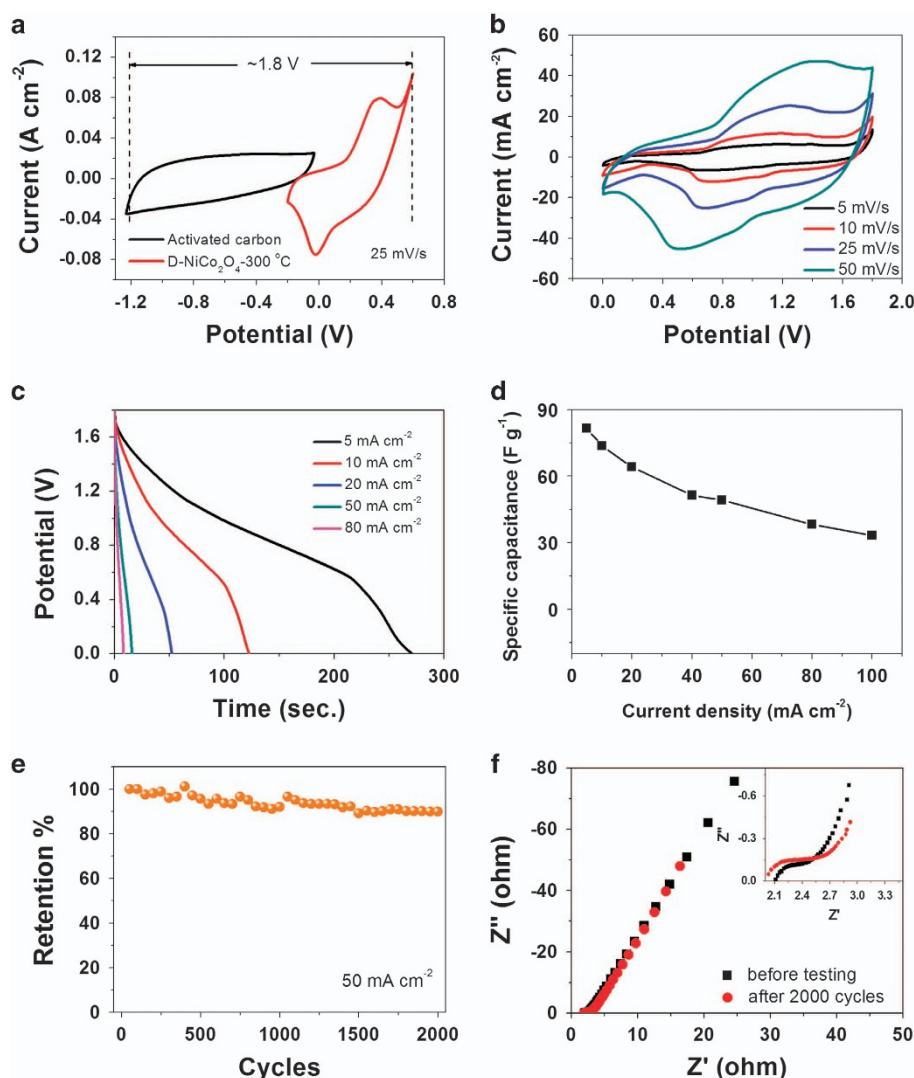
Figure 6 Electrochemical performance of $NiCo_2O_4$/AC asymmetric supercapacitor. Electrochemical evaluation of the $NiCo_2O_4$/activated carbon asymmetric supercapacitor device: (**a**) Comparative CV curves of $NiCo_2O_4$ and activated carbon electrodes performed in a three-electrode system. (**b**) C–V and (**c**) discharge curves of the asymmetric supercapacitor. (**d**) Calculated specific capacitance as a function of current density. (**e**) Cycling stability of the full cell. After 2000 cycles, 89.9% capacitance can still be retained, which is consistent with the results in the three-electrode system (90.5%). (**f**) electrochemical impedance spectroscopy curves measured before and after 2000 charge–discharge cycles.

shown in Figures 5e and f. After treating with hydrogen, the relative intensity of Ni^{2+} and Co^{2+} increased obviously, indicating the formation of oxygen vacancy. This can also be supported by the relative intensity of peak O2, which increased from 43.5 to 45.3% after hydrogenation. As oxygen vacancy is often considered to be electron donor, excess carriers are provided, resulting in improved electrical conductivity,[24] which agrees well with the Nyquist plots. As a result, the specific capacitance increased sequentially and reached the highest value after hydrogenation at low current density. In addition, the information of metal Ni and Co is observed (shown in Figures 5e and f). It means that some metals are reduced from metal oxide and decorate the surface of the oxides, which is similar with the assembly of conductive polymer such as PPy on the surface of materials to increase the conductivity and stability of electrochemical properties. This might also be one of the reasons for the explanation of the improvement of performance in this work. However, the poor crystalline structures cannot endure high current density, expansion of materials and changes in valence during charge and discharge. So, high current density performance and capacitance retention is not good enough and we need to optimize the treating parameters to keep a balance.

Performance of the NiCo$_2$O$_4$/AC asymmetric supercapacitor

To further evaluate the capacitive performance of the NiCo$_2$O$_4$ electrode for practical application, asymmetric supercapacitor device was fabricated using the D-NiCo$_2$O$_4$–300 °C and AC as the positive and negative electrodes in 6 M potassium hydroxide with one piece of cellulose paper as the separator according to the literature.[25] The mass of both active material and AC was controlled based on the principle of charge balance at the scanning rate of $25\,mV\,s^{-1}$ and the comparative CV curves of NiCo$_2$O$_4$ and AC electrodes performed in a three-electrode system are shown in Figure 6a. According to previous report,[25] the AC exhibits a typical characteristic of electric double-layer capacitance in an electrolyte of KOH aqueous solution within the range of -1.2–$0\,V$. Therefore, the working voltage of asymmetric supercapacitor device can be expected to reach to 1.8 V.

Figure 6b exhibits the C–V curves of the full cell and the cell voltage is as large as 1.8 V, which is almost twice that of conventional AC-based symmetric capacitors in aqueous electrolytes (0.8–1.0 V). Obviously, all the curves behave similar in shape and are much more rectangular as compared with those of NiCo$_2$O$_4$ electrode in three-electrode testing. Galvanostatic discharge performance under

different current densities is also illustrated in Figure 6c and the calculated specific capacitance at different current densities is displayed in Figure 6d. No obvious internal resistance (IR) drop is observed, indicating the fast I-V response of the device. Figure 6e exhibits the long-term cycling stability at the current density of $50\,mA\,cm^{-2}$ and 89.9% capacitance can still be retained after 2000 cycles, which is consistent with the results of half-cell in the three-electrode aqueous system(90.5%). Besides, electrochemical impedance spectroscopy spectra of the first and the 2000th cycle for the asymmetric supercapacitor device are exhibited in Figure 6f, and the inset is the magnified view at high frequency. We can see that there is a slight increase for the semicircle in the high-frequency range after the cycling stability test, indicating the increase of charge transfer resistance. However, the nearly overlap of the electrochemical impedance spectroscopy curves indicate the high stability of the asymmetric supercapacitor device. Ragone plot of the device calculated from the galvanostatic charge–discharge curves is also plotted in Figure 7 to demonstrate the relation between energy density and power density. The asymmetric supercapacitor device delivers a high energy density of $34.8\,Wh\,kg^{-1}$ at a power density of $464\,W\,kg^{-1}$. Even at a high power density of $5220\,W\,kg^{-1}$, the device still has an energy density of 11.6 $Wh\,kg^{-1}$. The performance is relatively better compared with various NiCo$_2$O$_4$-based asymmetric supercapacitors.[26–29]

CONCLUSION

In summary, double-shelled hollow sphere structure and low-temperature hydrogenation were proposed to achieve the integration of large specific surface area and high conductivity to collectively improve the capacitive performance of NiCo$_2$O$_4$ supercapacitors. The specific surface area of NiCo$_2$O$_4$ hollow spheres, fabricated by programmed coating of carbon spheres, was enlarged 50% (from 76.6 to $115.2\,m^2\,g^{-1}$) when their structure was transformed from single-shell to double-shell. Furthermore, AC impedance measurements demonstrated that the low-temperature hydrogenation greatly decreased both the internal resistance and the Warburg impedance. Consequently, a specific capacitance increase of $>62\%$, from 445 to $718\,F\,g^{-1}$, was achieved at a current density of $1\,A\,g^{-1}$. Underlying such great improvement, the evolution of chemical valence and defect states with co-increase of these two factors was explored through X-ray photoelectron spectroscopy. The full cell assembled using NiCo$_2$O$_4$ as positive electrode and AC as negative electrode demonstrated an energy density of $34.8\,Wh\,kg^{-1}$ at a power density of 464 $W\,kg^{-1}$. The simple and universal fabrication method presented herein is appropriate for many kinds of materials, including binary or ternary metal oxides with controllable multi-shelled microstructures for high performance supercapacitors, or even advanced Li-ion batteries.

CONFLICT OF INTEREST

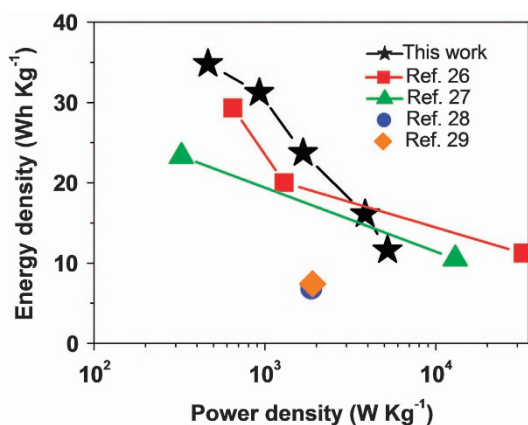The authors declare no conflict of interest.

Figure 7 Ragone plots of different supercapacitors from the galvanostatic charge–discharge curves.

1   Yu, L., Wu, H., Wu, T. & Yuan, C. Z. Morphology-controlled fabrication of hierarchical mesoporous $NiCo_2O_4$ micro-/nanostructures and their intriguing application in electrochemical capacitors. *RSC Adv.* **3**, 23709–23714 (2013).

2   Shakir, I., Sarfraz, M., Rana, U. A., Nadeem, M. & Al-Shaikha, M. A. Synthesis of hierarchical porous spinel nickel cobaltite nanoflakes for high performance electrochemical energy storage supercapacitors. *RSC Adv.* **3**, 21386–23189 (2013).

3   Zhang, G. Q. & Lou, X. W. General solution growth of mesoporous $NiCo_2O_4$ nanosheets on various conductive substrates as high-performance electrodes for supercapacitors. *Adv. Mater.* **25**, 976–979 (2013).

4   Wang, G. P., Zhang, L. & Zhang, J. J. A review of electrode materials for electrochemical supercapacitors. *Chem. Soc. Rev.* **41**, 797–828 (2012).

5   Padmanathan, N. & Selladurai, S. Controlled growth of spinel $NiCo_2O_4$ nanostructures on carbon cloth as a superior electrode for supercapacitors. *RSC Adv.* **4**, 8341–8349 (2014).

6   Yuan, C. Z., Li, J. Y., Hou, L. R., Zhang, X. G., Shen, L. F. & Lou, X. W. Ultrathin mesoporous $NiCo_2O_4$ nanosheets supported on Ni foam as advanced electrodes for supercapacitors. *Adv. Funct. Mater.* **22**, 4592–4597 (2012).

7   Zou, R. J., Xu, K. B., Wang, T., He, G. J., Liu, Q., Liu, X. J., Zhang, Z. Y. & Hu, J. Q. Chain-like $NiCo_2O_4$ nanowires with different exposed reactive planes for high-performance supercapacitors. *J. Mater. Chem. A* **1**, 8560–8566 (2013).

8   Zhou, W. W., Kong, D. Z., Jia, X. T., Ding, C. Y., Cheng, C. W. & Wen, G. W. $NiCo_2O_4$ nanosheet supported hierarchical core-shell arrays for high-performance supercapacitors. *J. Mater. Chem. A* **2**, 6310–6315 (2014).

9   Shen, L. F., Che, Q., Li, H. S. & Zhang, X. G. Mesoporous $NiCo_2O_4$ nanowire arrays grown on carbon textiles as binder-free flexible electrodes for energy storage. *Adv. Funct. Mater.* **24**, 2630–2637 (2014).

10 Deng, F. Z., Yu, L., Cheng, G., Lin, T., Sun, M., Ye, F. & Li, Y. F. Synthesis of ultrathin mesoporous $NiCo_2O_4$ nanosheets on carbon fiber paper as integrated high-performance electrodes for supercapacitors. *J. Power Sources* **251**, 202–207 (2014).

11 Yu, X. Y., Yao, X. Z., Luo, T., Jia, Y., Liu, J. H. & Huang, X. J. Facile synthesis of urchin-like $NiCo_2O_4$ hollow microspheres with enhanced electrochemical properties in energy and environmentally related applications. *ACS Appl. Mater. Inter.* **6**, 3689–3695 (2014).

12 Yuan, C. Z., Li, J. Y., Hou, L. R., Lin, J. D., Pang, G., Zhang, L. H., Lian, L. & Zhang, X. G. Template-engaged synthesis of uniform mesoporous hollow $NiCo_2O_4$ sub-microspheres towards high-performance electrochemical capacitors. *RSC Adv.* **3**, 18573–18578 (2013).

13 Xu, K. B., Li, W. Y., Liu, Q., Li, B., Liu, X. J., An, L., Chen, Z. G., Zou, R. J. & Hu, J. Q. Hierarchical mesoporous $NiCo_2O_4@MnO_2$ core-shell nanowire arrays on nickel foam for aqueous asymmetric supercapacitors. *J.Mater. Chem. A* **2**, 4795–4802 (2014).

14 Peng, S. J., Li, L. L., Li, C. C., Tan, H. T., Cai, R., Yu, H., Mhaisalkar, S., Srinivasan, M., Ramakrishna, S. & Yan, Q. Y. *In situ* growth of $NiCo_2S_4$ nanosheets on graphene for high-performance supercapacitors. *Chem. Comm.* **49**, 10178–10180 (2013).

15 Yuan, C. Z., Wu, H. B., Xie, Y. & Lou, X. W. Mixed transition-metal oxides: design, synthesis, and energy-related applications. *Angew. Chem. Int. Ed.* **53**, 1488–1504 (2014).

16 Zhang, Y. F., Ma, M. Z., Yang, J., Su, H. Q., Huang, W. & Dong, X. C. Selective synthesis of hierarchical mesoporous spinel $NiCo_2O_4$ for high-performance supercapacitors. *Nanoscale* **6**, 4303–4308 (2014).

17 Yang, Z. H., Xu, F. F., Zhang, W. X., Mei, Z. S., Pei, B. & Zhu, X. Controllable preparation of multishelled NiO hollow nanospheres via layer-by-layer self-assembly for supercapacitor application. *J. Power Sources* **246**, 24–31 (2014).

18 Hu, L. F., Wu, L. M., Liao, M. Y., Hu, X. H. & Fang, X. S. Electrical transport properties of large, individual $NiCo_2O_4$ nanoplates. *Adv. Funct. Mater.* **22**, 998–1004 (2012).

19 Cheng, J., Cao, G. P. & Yang, Y. S. Characterization of sol–gel-derived NiO_x xerogels as supercapacitors. *J. Power Sources* **159**, 734–741 (2006).

20 Lu, X. H., Wang, G. M., Zhai, T., Yu, M. H., Gan, J. Y., Tong, Y. X. & Li, Y. Hydrogenated TiO_2 nanotube arrays for supercapacitors. *Nano Lett.* **12**, 1690–1696 (2012).

21 Wang, J. P., Wang, Z. Y., Huang, B. B., Ma, Y. D., Liu, Y. Y., Qin, X. Y., Zhang, X. Y. & Dai, Y. Oxygen vacancy induced band-gap narrowing and enhanced visible light photocatalytic activity of ZnO. *ACS Appl. Mater. Inter.* **4**, 4024–4030 (2012).

22 Li, H. B., Yu, M. H., Wang, F. X., Liu, P., Liang, Y., Xiao, J., Wang, C. X., Tong, Y. X. & Yang, G. W. Amorphous nickel hydroxide nanospheres with ultrahigh capacitance and energy density as electrochemical pseudocapacitor materials. *Nat. Commun.* **4**, 1894 (2013).

23 Cui, B., Lin, H., Liu, Y. Z., Li, J. B., Sun, P., Zhao, X. C. & Liu, C. J. Photophysical and photocatalytic properties of core-ring structured $NiCo_2O_4$ nanoplatelets. *J. Phys. Chem. C* **113**, 14083–14087 (2009).

24 Shen, L. F., Uchaker, E., Zhang, X. G. & Cao, G. Z. Hydrogenated $Li_4Ti_5O_{12}$ nanowire arrays for high rate lithium Ion batteries. *Adv. Mater.* **24**, 6502–6506 (2012).

25 Zhou, C., Zhang, Y. W., Li, Y. Y. & Liu, J. P. Construction of high-capacitance 3D CoO@polypyrrole nanowire array electrode for aqueous asymmetric supercapacitor. *Nano Lett.* **13**, 2078–2085 (2013).

26 Chen, H. C., Jiang, J. J., Zhang, L, Qi, T., Xia, D. D. & Wan, H. Z. Facilely synthesized porous NiCo2O4 flowerlike nanostructure for high-rate supercapacitors. *J. Power Sources* **248**, 28–36 (2014).

27 Wang, X., Liu, W. S., Lu, X. H. & Lee, P. S. Dodecyl sulfate-induced fast faradic process in nickel cobalt oxide-reduced graphite oxide composite material and its application for asymmetric supercapacitor device. *J. Mater. Chem.* **22**, 23114–23119 (2012).

28 Tang, C. H., Tang, Z. & Gong., H. Hierarchically porous Ni-Co oxide for high reversibility asymmetric full-cell supercapacitors. *J. Electrochem. Soc.* **159**, A651–A656 (2012).

29 Ding, R., Qi, L., Jia, M. J. & Wang, H. Y. Facile and large-scale chemical synthesis of highly porous secondary submicron/micron-sized NiCo2O4 materials for high-performance aqueous hybrid AC-NiCo2O4 electrochemical capacitors. *Electrochim. Acta* **107**, 494–502 (2013).

Supplementary Information accompanies the paper on the NPG Asia Materials website (http://www.nature.com/am)